Geologic analyses of Shuttle Imaging Radar (SIR-B) data of Kilauea Volcano, Hawaii

LISA GADDIS*
PETE MOUGINIS-MARK } *Planetary Geosciences Division, Hawaii Institute of Geophysics, University of Hawaii, Honolulu, Hawaii 96822*
ROBERT SINGER *Lunar and Planetary Laboratory, University of Arizona, Tucson, Arizona 85721*
VERNE KAUPP *Department of Engineering, University of Arkansas, Fayetteville, Arkansas 72701*

ABSTRACT

Analyses of imaging radar data of volcanic terranes on Earth and Venus have emphasized the need for a clearer understanding of how these data can be most effectively used to accomplish important volcanological goals, including the interpretation of eruptive styles and the characterization of the geologic history of volcanic centers. The second Shuttle Imaging Radar experiment (SIR-B) obtained two digital images over the summit caldera and the Southwest Rift Zone of Kilauea Volcano in 1984. Our geologic analyses of these images indicate that SIR-B data are particularly useful for delineating the distribution and surface textural variations of a'a lava flows, for mapping large-scale topographic features with radar-facing slopes, and for identifying an areally extensive pyroclastic deposit. Analyses of the SIR-B data of Kilauea, however, do not permit unambiguous identification of landforms such as pahoehoe lava flows, cinder cones, and fissures. Although separation of low-return units such as pahoehoe lava flows and adjacent pyroclastic ash is not greatly improved using standard image-enhancement techniques, the texture-analysis technique applied here did facilitate discrimination of such smooth-surfaced volcanic deposits. Although analyses of the SIR-B data permit a generally accurate interpretation of the eruptive history of Kilauea, the inability to distinguish low-return pahoehoe flows results in misinterpretation of several aspects of Kilauea volcanism, suggesting that caution should be exercised in the interpretation of SAR data of volcanic terranes.

INTRODUCTION

Geologic analyses of remote-sensing data acquired over volcanic terranes on the Earth and on the terrestrial planets have provided important chemical and physical constraints on our understanding of the occurrence and context of basaltic volcanism in the Solar System. Compositional, stratigraphic, and lithologic information obtained from remote-sensing techniques such as reflectance spectroscopy (Pieters and others, 1973; Pieters, 1978; McCord and others, 1981; Singer, 1985), and imaging at visible, near-infrared, thermal (Carr and others, 1977; Kieffer and others, 1977), and radar wavelengths (Schaber and others, 1975; Zisk and others, 1977; Gaddis and others, 1985a) have permitted comparison of the processes and products of eruptions, and interpretation of eruptive histories of volcanic terranes which would otherwise be inaccessible to us. In some areas of the Earth and on the surface of Venus, for example, the operation of remote-sensing systems employing short wavelengths (0.4 to 12 μm) is hampered by the presence of fog, clouds, and/or rain. In recent years, this limitation has been overcome by the use of longer-wavelength, orbital imaging synthetic aperture radar (SAR) sensors on Earth such as those of the Seasat and the two Shuttle Imaging Radar systems (SIR-A and SIR-B; Table 1). These L-band (23-cm wavelength) SAR systems, virtually unaffected by weather conditions and operable at any time of day, have provided synoptic data over several volcanically active areas of Earth (Elachi and others, 1980; Farr and others, 1981; Blom and other, 1982; Fielding and others, 1986; Kaupp and others, 1986), many of which are commonly obscured by clouds. In addition, analysis of United States Earth-based and Soviet orbital radar images of the cloud-covered surface of Venus has identified many probable volcanic features and units (Masursky and others, 1980; Campbell and others, 1984; Barsukov and others, 1986; Basilevsky and others, 1986). The surface of Venus is currently scheduled to be more closely examined by the orbital imaging SAR system of NASA's *Magellan* spacecraft.

To understand the character of volcanic eruptions and their products as observed by SAR systems, we can conduct geologic analyses of imaging radar data acquired over accessible volcanic terranes on Earth. Kilauea Volcano, Hawaii, is an excellent site for such an analysis for a number of reasons, including its accessibility, its relative lack of vegetation, and the variety of lithologies, morphologies, and ages of volcanic units present. In 1984, two SIR-B SAR images were acquired over the summit caldera and Southwest Rift Zone of Kilauea Volcano at 28°- and 48°-incidence angles (the angle between the transmitted/incident wave and the normal to the ground; Fig. 1).

Preliminary analyses of the SIR-B data of Kilauea indicated that many volcanic landforms could be readily identified on these data, including large-scale topographic features such as fault scarps and crater rims which were facing the radar antenna, a'a lava flows, and ash deposits (Gaddis and others, 1985b; Kaupp and others, 1986). Difficulty in recognizing pahoehoe lava flows, and small cinder cones, spatter ramparts, and

TABLE 1. NASA ORBITAL RADAR MISSIONS

Mission	Year	Wavelength	Incidence angle	Resolution
Seasat	1978	L-Band	23°	25 m
SIR-A	1981	L-Band	47°	40 m
SIR-B	1984	L-Band	15° to 60°	25 m
SIR-C*	1990	X-, C-, L-Band	15° to 60°	25 m
Magellan	1989	S-Band	15° to 45°	150 m

*Four polarizations (HH, HV, VV, VH) at L- and C-band; only VV at X-band.

*Present address: Department of Geology, Arizona State University, Tempe, Arizona 85287.

Geological Society of America Bulletin, v. 101, p. 317–332, 17 figs., 3 tables, March 1989.

fissures associated with eruptive centers, however, precludes an accurate interpretation of the character of volcanism near Kilauea on the basis of the SIR-B data alone. To facilitate the use of SAR data in the geologic analysis of less accessible volcanic terranes, we present a summary of volcanic landforms of Kilauea as they are seen on the SIR-B images, the results of image enhancement and analysis (that is, image smoothing, unit mapping, and texture analysis) of the SIR-B data to improve unit discrimination, and a discussion of the advantages and limitations of the SIR-B data for characterizing volcanism at Kilauea.

Radar as a Geologic Tool

Geologic analyses of SAR images are commonly based on the ability to relate backscatter intensity on an image to a specific surface or feature. Radar backscatter intensity is influenced by system parameters and terrane properties (Sabins, 1986; Elachi and others, 1986). Radar system parameters include wavelength, incidence angle, and polarization of the transmitted signal. For radar systems which use directly polarized radar energy (such as the SIR-B sensor), backscatter intensity is generally determined by the amount of surface scattering. Terrane properties which have the most influence on radar backscatter include topographic slopes, surface roughness on the scale of the radar wavelength, and electrical properties of the surface materials (described by the complex dielectric constant). Topographic landforms with slopes oriented toward the radar antenna generally have high backscatter intensities because they are preferentially illuminated; although backscatter is higher at smaller incidence angles, images are distorted by foreshortening and/or layover at small angles of incidence (less than about 30°) in steep terranes.

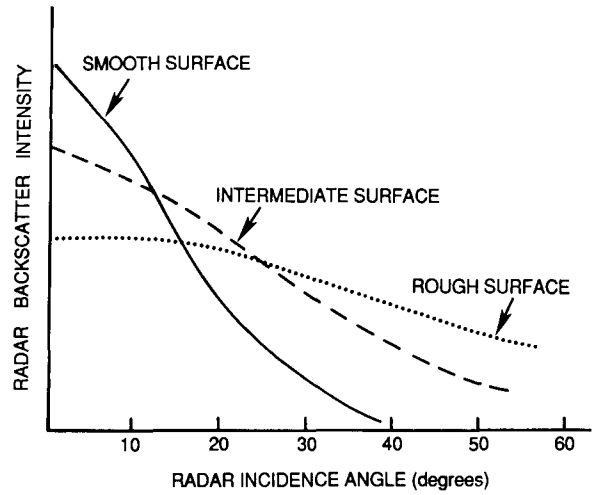

Figure 2. The theoretical radar backscatter versus incidence-angle response for surfaces with different roughnesses (after Cimino and others, 1986). A radar-smooth surface has an average roughness smaller than the wavelength, whereas a radar-rough surface has an average roughness comparable to, or greater than, the wavelength.

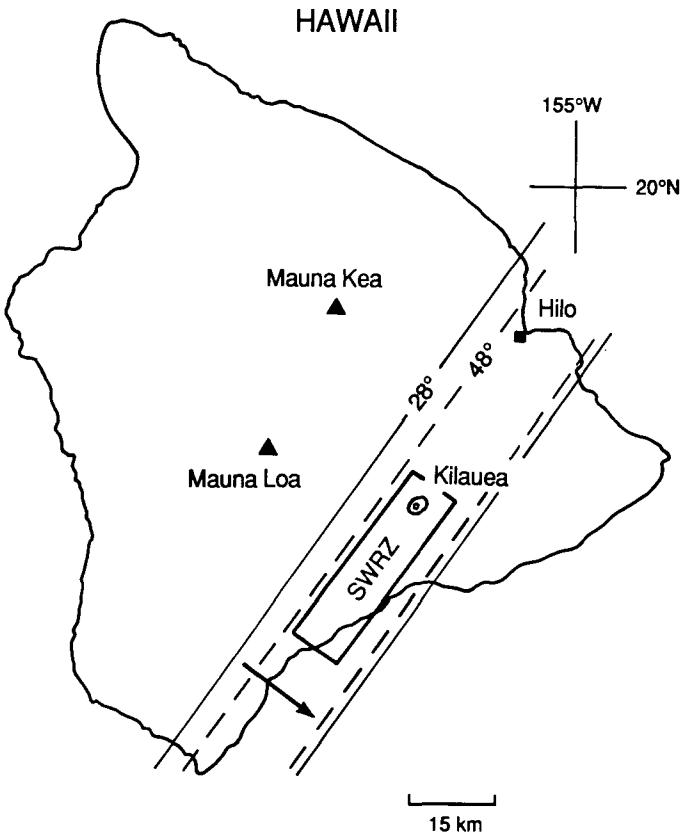

Figure 1. Sketch map of Hawaii. SIR-B collected digital data along the two ground swaths shown: the solid line outlines the image acquired at a 28°-incidence angle (data take 99.2), whereas the dashed line marks the 48°-incidence-angle image (data take 115.2). The radar illumination direction (arrow) is toward the southeast. The area shown in Figure 3, the Kilauea summit and Southwest Rift Zone (SWRZ), is also outlined.

In radar surveys, roughness is a measure of the irregularity of the surface (both vertical and horizontal) compared with the radar wavelength. Although vertical relief (typically cited as the standard deviation of the surface height variations or "root mean square" heights; Ulaby and others, 1982) is only an approximation of the complex geometries often found in natural terranes, it is a commonly used measure of surface roughness. On radar images, geologic surfaces can be classified as smooth, intermediate, or rough, relative to the radar wavelength and angle of incidence; the relationship between radar incidence angle and backscatter intensity for increasingly rough surfaces is shown in Figure 2. Smooth surfaces produce mirrorlike or specular reflections in which radar energy is returned at an angle equal and opposite to the incidence angle. Because significant backscatter from smooth surfaces is received only at very small (almost vertical) angles of incidence or from slopes oriented toward the radar antenna, specular reflectors appear dark on radar images. Surfaces of intermediate roughness (with moderate brightness on radar images) scatter incident energy diffusely in all directions, with the largest component reflected at an angle approximately equal to the incidence angle. A rough surface is a diffuse scatterer, reflecting energy equally in all directions; rough surfaces scatter diffusely at relatively uniform intensity regardless of the angle of incidence. Because rough surfaces return the most energy to the receiver, they are bright features on radar images.

The complex dielectric constant is a representation of the physical state (for example, density, porosity) and composition of geologic materials (Ulaby and others, 1981). The dielectric constant is most strongly influenced by moisture content; as dielectric properties of soils and rocks increase as a direct function of moisture content, wet materials produce backscatter of a higher intensity than do dry materials of the same type. As observed in the 47°-incidence angle SIR-A images of the Sahara, L-band radar is capable of penetrating dry sand to depths of at least 1.5 m (Schaber and others, 1986). In the Sahara, the occurrence of smooth-

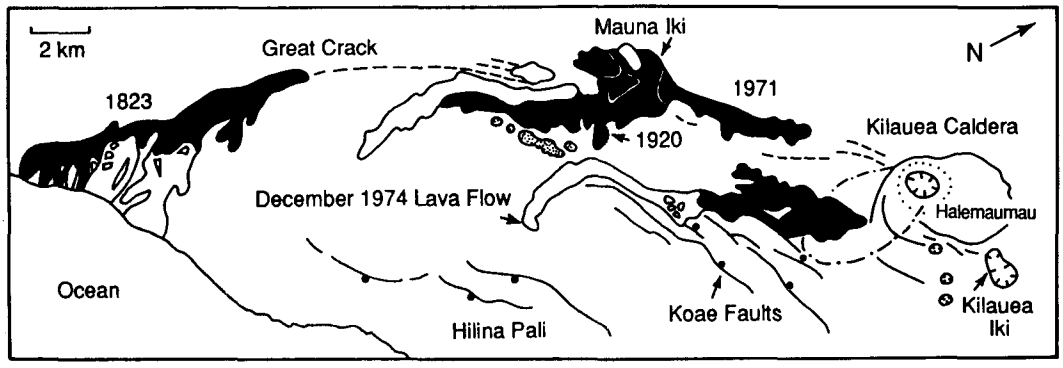

Figure 3. Map of the Kilauea summit and SWRZ showing major volcanic landforms: pahoehoe flows are shaded in black; a'a flows are outlined; the 1790 (dot-dashed line) and 1924 (dotted line) pyroclastic deposits are also outlined; dashed lines mark SWRZ fissures; faults are outlined with dots marking the downthrown side; pit craters are outlined with inward tickmarks; cones of the Kamakaia Hills are dotted.

surfaced, hyperarid, unconsolidated sand overlying a shallowly buried stream channel has permitted surface penetration and reflection of radar energy from subsurface rocks. In the absence of a subsurface reflector, backscatter from a thick (at least several meters deep), dry, sandy layer is low (dark) due to attenuation (absorption) of the radar energy (Schaber and others, 1986). For dry, coherent volcanic materials with limited compositional variability, such as the majority of those of the summit and Southwest Rift Zone of Kilauea Volcano, surface roughness may be considered to have the strongest influence on backscatter intensity.

Geologic Setting

SIR-B radar coverage of Hawaii extends northeastward from the southern tip of the island over the Southwest Rift Zone and summit caldera of Kilauea Volcano to the town of Hilo (Fig. 1). Kilauea Volcano is a broad, low-relief (1,200-m-high) volcanic shield located at the base of the southeastern side of the larger Mauna Loa shield (4,000 m high).

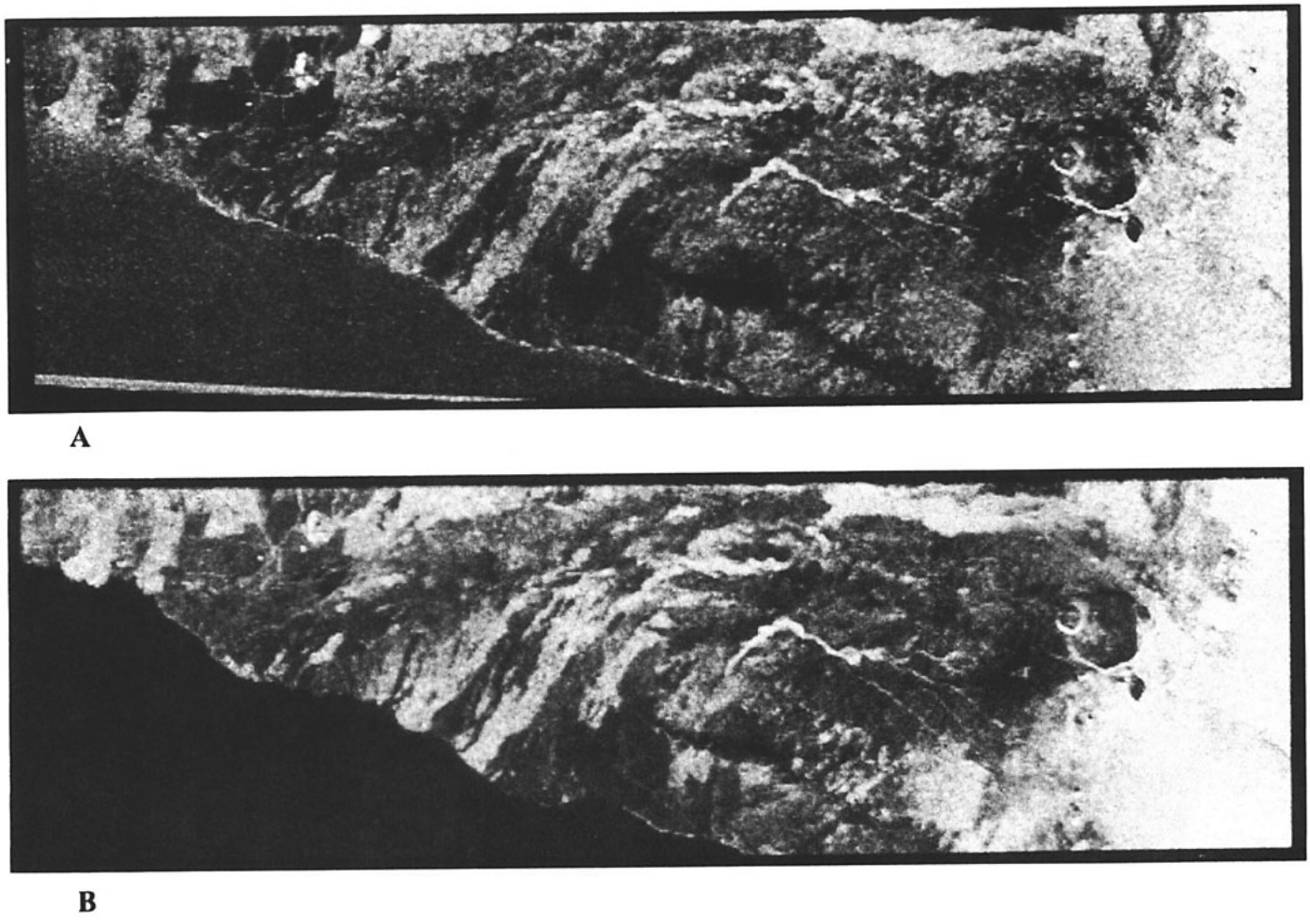

Figure 4. Contrast-enhanced segments of the SIR-B images of Kilauea: (A) was acquired at a 28°-incidence angle. The area shown (comparable to that of Fig. 3) extends from Kilauea Caldera (at right) southwest along the SWRZ to the ocean. The radar look direction is top to bottom (to southeast) for each image.

Recent volcanic activity at Kilauea is characterized by quiescent effusion of very fluid basaltic lavas with small amounts of associated gas (Macdonald and others, 1983). Although fire-fountaining is often observed, only two violently explosive eruptions have occurred near Kilauea in historic times: the extremely energetic (by Hawaiian standards) phreatomagmatic eruption of Kilauea Caldera in 1790 and the less energetic phreatic eruption of Halemaumau in 1924 (Decker and Christiansen, 1984).

SIR-B coverage included two major structural components of Kilauea: the summit caldera complex and the Southwest Rift Zone (Fig. 3). The summit is dominated by Kilauea Caldera (4.0 km across, 120 m deep) which is ringed by a series of arcuate step faults on the northeastern and western sides, whereas the southern rim is a low, ash-mantled rise. The pit crater Halemaumau (900 m diameter) has been the site of most of the recent volcanic activity of the Kilauea summit. Much of the floor of Kilauea Caldera is covered with pahoehoe lava flows (ranging in age from prehistoric to young; the most recent summit eruption was in September of 1982) and mantling deposits of ash produced during the 1790 and 1924 explosive eruptions of Halemaumau. An additional pyroclastic deposit, erupted in 1959, is associated with the Kilauea Iki crater and cone located just to the east of Kilauea Caldera.

The Southwest Rift Zone (SWRZ), extending southward from Kilauea Caldera to the ocean, is bounded to the east by the northwest-facing, 10-m-high normal faults of the Koae fault system. Farther south, scarps of the southeast-facing Hilina Pali are as much as 500 m high. Historic volcanic eruptions of the SWRZ originated along fissures such as the Great Crack (as much as 15 m wide) and those of the upper rift zone (as much as 10 m wide) near Kilauea Caldera (Holcomb, 1987; Fig. 3). Many of these flows consist of pahoehoe near the vent and grade to a'a along the length of the flow. Vent areas are commonly marked by features such as cinder cones, spatter ramparts, and low lava shields (for example, Mauna Iki).

VOLCANIC LANDFORM CHARACTERIZATION

A major objective of many geologic analyses of volcanic terranes has been the characterization of landforms indicative of eruption styles and emplacement mechanisms (for example, Basaltic Volcanism Study Project, 1981, ch. 5). Morphologic analyses of a variety of volcanic landforms, including topographic features (Nakamura and others, 1980; Wood, 1984), pyroclastic deposits (Walker, 1973), and effusive products (Hulme, 1974; Baloga and Pieri, 1986; Peterson and Tilling, 1980), are conducted to understand the importance of factors such as tectonics, topography, magma characteristics, and environmental conditions and their influence on eruption and emplacement style. To understand the utility of SAR data for volcanic landform characterization, the following sections describe SIR-B radar signatures of many of the major volcanic landforms of Kilauea (Fig. 4) and attempt to identify the characteristics of the surface materials which most strongly influenced those signatures.

Topographic Features

Topographic features with identifiable radar signatures on the SIR-B data of Kilauea include the summit caldera, the interior pit crater Halemaumau, the adjacent pit crater of Kilauea Iki, the Koae faults (Fig. 5), and portions of the Great Crack. Each of these features has an enhanced (brighter) radar backscatter due to topographic relief of 10 m or more and slopes oriented approximately perpendicular to the SIR-B radar antenna. Topographic features which are not readily detectable on the SIR-B radar images of the SWRZ include the low (40-m-high), broad lava shield of Mauna Iki; the Kamakaia Hills, a complex of small (30-m-high) cinder

Figure 5. Scarps (~10 m high) of the Koae faults (looking southwest). The December 1974 flow can be seen on the right in the distance.

Figure 6. The prehistoric spatter-and-cinder cones of the Kamakaia Hills. The larger cone in the foreground is ~30 m high.

Figure 7. An aerial view of fissures (as much as 5 m wide) of the upper SWRZ, just southwest of Kilauea Caldera (note road for scale). These fissures have been partly filled by pahoehoe lavas of the September 1971 flow.

cones (Fig. 6); and the extensive set of fractures (which range in width from a centimeter to as much as 10 m) to the south and west of Kilauea Caldera (Fig. 7). Although gentle slopes and the predominance of smooth, low-return pahoehoe lavas may inhibit identification of Mauna Iki, the Kamakaia Hills, although observable on the SIR-B images as small, isolated bright patches, are not recognizable as cinder cones. Similarly, the network of narrow fractures near Kilauea Caldera is represented by only two short, bright traces on the SIR-B data; these traces appear to have been produced by fissures greater than about 5 m in width oriented approximately perpendicular to the illumination direction of the radar. Few of the many fissures of the SWRZ are both large enough and oriented properly to have bright signatures on the SIR-B data.

Pyroclastic Deposits

Dark, low-return landforms on the SIR-B images include slopes facing away from the radar antenna (for example, the Hilina Pali), smooth-surfaced units such as relatively unconsolidated pyroclastic deposits, and pahoehoe lava flows with glassy surfaces. One of the darkest units on the SIR-B data is associated with an extensive tephra deposit (the Keanakakoi Formation of Wentworth, 1938) which blankets the area immediately to the south of Kilauea Caldera and extends outward about 5 km. This deposit, emplaced during the 1790 explosive eruption of Halemaumau, consists of numerous thin layers of sandy ash with occasional blocks and boulders up to 0.5 m in diameter and a total thickness of as much as 9 m within the caldera (Fig. 8; Malin and others, 1983). The darkness of this unit on the SIR-B image is comparable to that of a smooth, dry, sandy soil (Berlin and others, 1986), suggesting that the presence of scattered blocks and boulders on and within this deposit has little or no effect on the radar signature. Geologic analyses of SIR-A and SIR-B radar data acquired over the Sahara indicate that dark returns from smooth, thick (up to several meters deep), dry, sandy soils result from penetration and absorption of the radar signal within the layer (Schaber and others, 1986). The relative contributions of quasi-specular scattering from the smooth surface and subsurface attenuation to the dark radar signature of the 1790 deposit cannot be determined with these data.

Two additional pyroclastic deposits of Kilauea have less-distinctive signatures on the SIR-B data. The phreatic eruption of Halemaumau in 1924 produced an ejecta deposit consisting of scattered fragments of host rock ranging in size from sand-sized ash particles to 1-m-diameter boulders (Fig. 9; Macdonald and others, 1983; Decker and Christiansen, 1984). Field observations of this unit indicate that it is a thin (less than 10 cm near Halemaumau; "trace" deposits of Decker and Christiansen, 1984) blanket of debris scattered over pre-existing units. In the SIR-B data, this unit cannot be directly correlated with the irregular "halo" of radar-bright material surrounding Halemaumau (Figs. 4 and 10). Because the observed SIR-B radar signatures correspond most closely to those of the underlying volcanic units, we conclude that the blocks and boulders of the 1924 phreatic eruption are too broadly scattered to have a strong influence on the radar backscatter from this area.

In contrast to the radar-dark return of the 1790 deposit, the 1959 pyroclastic deposit southwest of Kilauea Iki crater produced a mottled, moderately dark return on the SIR-B images. This unit, consisting of cinder, spatter, and pumice distributed up to 4 km downwind (south-southwest) of the eruption site, is up to 1 m thick at a 1-km distance from the vent (Macdonald and others, 1983). The proximity of rain-forest vegetation southwest of the vent at Kilauea Iki prevents examination of the distal portion of the 1959 deposit on the SIR-B images and precludes a determination of the influence of subsurface units on radar signatures of this deposit. It is possible, however, that the semi-consolidated (for example, clotted) nature of the cinder and spatter of much of this unit has inhibited subsurface penetration and attentuation of the SIR-B signal, resulting in a low-return unit with a slightly higher backscatter than that of the 1790 tephra deposit.

Source Vents

The lack of correspondence between the 1924 phreatic deposit and the irregular "halo" around Halemaumau (particularly bright to the north and east) indicates that a factor other than surface roughness is contributing to the radar backscatter in this area. For example, examination of the schematic map and the SIR-B images in Figure 10 shows that the distribution of the brighter areas of the halo does not correspond to those of mapped lava flows. Two explanations for the origin of the irregular halo are plausible at this time: (1) the 2- to 3-m-high spatter ramparts (east-west–trending) of the April 1982 vent (Fig. 11A) and the north rim of Halemaumau (with a northward slope of about 10°) have radar-facing

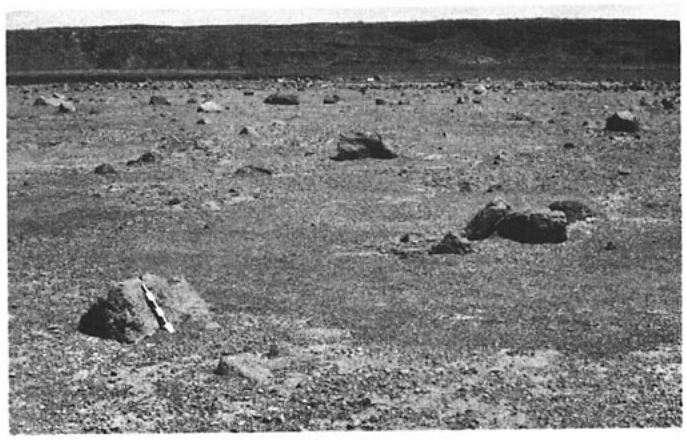

Figure 8. The surface of the 1970 ash deposit (~0.5 km southwest of Halemaumau) looking north. Here the ash has a smooth, pebbly surface, with sandy material ~1 cm below the surface. Blocks from the 1924 phreatic eruption are also scattered across this surface; note 30-cm ruler for scale.

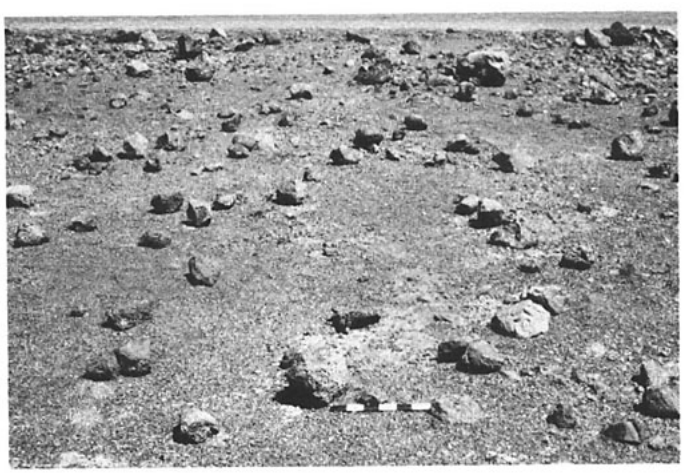

Figure 9. Blocks and boulders of the 1924 phreatic eruption of Halemaumau (located ~0.25 km southeast of Halemaumau). The ruler is 30 cm long.

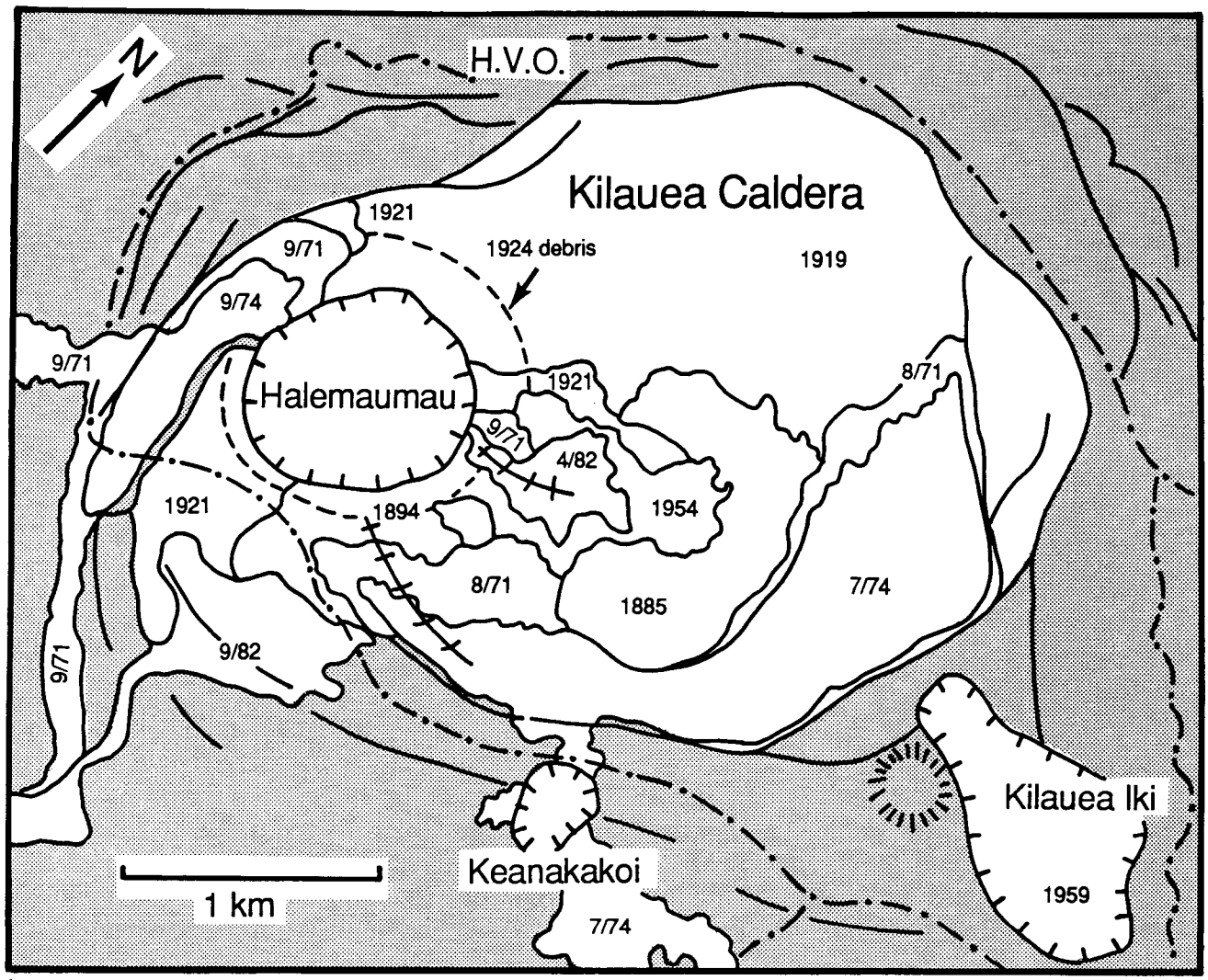

A

Figure 10. Kilauea Caldera: (A) map of major features (faults, fissures, cones, craters) and lava flows in the caldera floor (the flow eruption month and/or year are shown); roads are marked with a dot-dashed line, fissures are hachured. "H.V.O." is the Hawaii Volcano Observatory of the U.S. Geological Survey. Contrast-enhanced segments of the (B) 28° and (C) 48°-incidence-angle SIR-B data for the same area are also shown. The radar look direction is top to bottom (southeast) in these images.

slopes that are of sufficient relief to enhance the backscatter of these areas; (2) fumarolic activity, intermittently occurring all around Halemaumau but particularly prominent to the east and southeast (Fig. 11B), may have increased the backscatter of these areas due to the precipitation of mineral salts and/or water. Determination of the relative contributions of these factors cannot be made without additional field reconnaissance and sampling in this area.

Lava Flows

Surface cover of the summit and SWRZ of Kilauea consists primarily of the products of effusive volcanic eruptions, with a distribution of about 67% tube-fed pahoehoe, 14% surface-fed pahoehoe, and 16% a'a (Holcomb, 1987). Lava flows near the summit of Kilauea are commonly tube-fed pahoehoe flows, whereas surface-fed pahoehoe flows occur in near-vent areas along the rift zones, and a'a lava flows predominantly occur downslope (southeast) of the rift zones. A'a lavas are often observed at the distal portions of flows erupted as both tube- and surface-fed pahoehoe; such a'a is produced by cooling and crystallization of pahoehoe lava as it moves farther from the source vent (Peterson and Tilling, 1980; Kilburn, 1981).

In Hawaii, pahoehoe lavas are commonly very fluid, with low viscosities (200 to 400 Pa s; Shaw, 1969) and only small amounts of dissolved gases (<0.5 wt%; Greenland, 1987). As a result, pahoehoe flows have smooth, glassy, gently undulating surfaces typical of a rapidly cooled fluid. With such surfaces, pahoehoe flows act as specular reflectors and thus exhibit very low backscatter on the SIR-B images. When young, relatively unaltered pahoehoe lava flows occur in proximity to other dark, low-return volcanic landforms such as the 1790 pyroclastic deposit, they cannot be readily differentiated on the SIR-B images. For example, the July

B

Figure 10. (*Continued*).

C

Figure 10. (*Continued*).

1974 flow in the southeastern floor of Kilauea Caldera and the smaller September 1982 flow near the south rim are unrecognizable on the SIR-B data (Fig. 10).

In contrast to pahoehoe lava flows, the brightest geologic units on the SIR-B data are the a'a lava flows in the SWRZ (Figs. 3 and 4). A'a flows are so rough to the 23-cm SIR-B wavelength that they act as diffuse scatterers, deflecting the incident radar energy in all directions; this type of scattering, which occurs at all incidence angles, produces the brightest returns observed on the SIR-B data. A'a flow units typically consist of extremely irregular, jagged, clinkery surfaces overlying a massive inner core of lava, which is itself underlain by a thinner layer of clinker (Stearns, 1985). Clinker fragments range from less than a centimeter to a meter in diameter, and they may become larger and more rounded as distance from the vent increases along the flow. Accretionary lava balls as much as 2.5 m in diameter are often the largest surficial components of a'a flows; these balls form as a solid block of lava is rolled along on the surface of a flow, accumulating layers of viscous, plastic lava (Wentworth and Macdonald, 1953).

A'a lava flows of the SWRZ are 0.5 m to about 4 m thick and range in age from recent (1974) to prehistoric (as much as 1,500 yr old; Holcomb, 1987). The majority of a'a flows mapped by Holcomb (1980) in the SWRZ, irrespective of age and/or vegetation cover, can be readily distinguished on the SIR-B images. Exceptions to this are flows (200 to 700 yr old; Holcomb and others, 1986) of the north-central SWRZ which have been mantled by wind-blown deposits (generally only a few centimeters thick) presumably derived from weathering of basalts and pyroclastic deposits near the Kilauea summit.

Clearly, the SIR-B radar has separated pahoehoe flows from a'a flows on the basis of surface texture or roughness. To determine the scale of roughness at which this separation occurs, we have examined the December 1974 lava flow in the north-central SWRZ (Figs. 3 and 12A). This

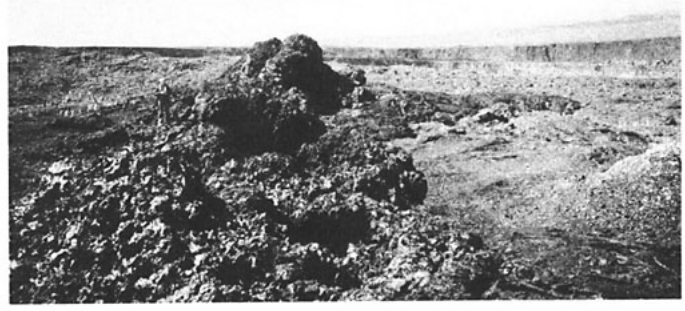

A

B

Figure 11. View of the floor of Kilauea Caldera near Halemaumau: (A) spatter ramparts of the April 1982 eruption (2 to 3 m high; view to southwest); (B) fumaroles located southeast of Halemaumau near the fissure vents of the July 1974 eruption (view to northwest).

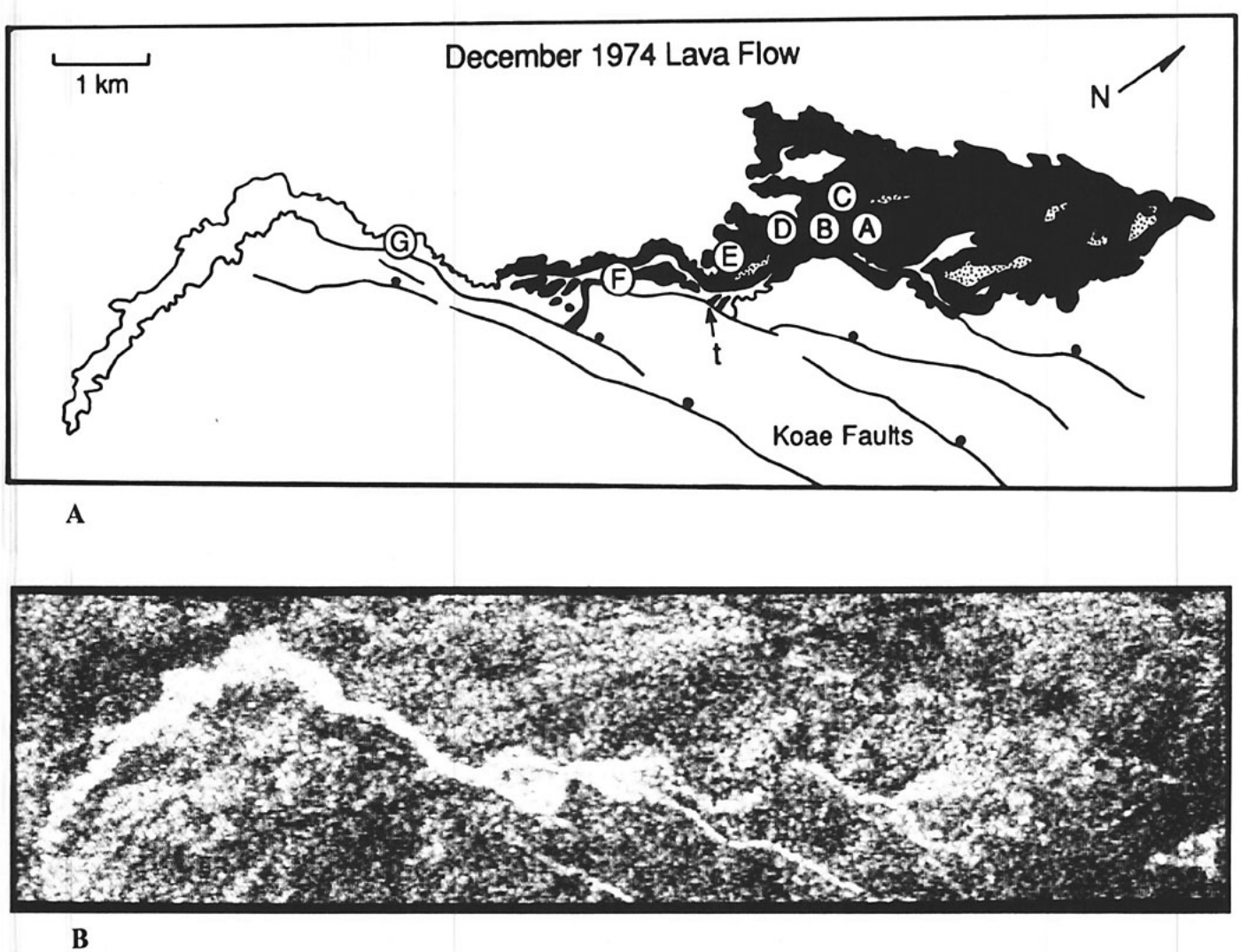

Figure 12. The December 1974 lava flow: (A) map of the distribution of pahoehoe (dark) and a'a (outlined) lavas, kipukas (dotted areas), and sites (lettered A through G) of surface-roughness measurements; (B) contrast-enhanced 48° SIR-B image. Note that the pahoehoe flow portion is difficult to distinguish on the radar image; the flow is more easily observed near the pahoehoe-to-a'a transition zone (marked with a "t"). The radar look direction is to the southeast (top to bottom).

flow erupted as pahoehoe from fissures 2 km south of Kilauea Caldera, cooled, and became more viscous as the flow moved, fragmented into plates and clinker, and became a'a about 5 km from the vent. In the SIR-B image (Fig. 12B), only the rougher a'a portion of this flow is clearly visible.

The degree of roughness which separates a "radar-smooth" from a "radar-rough" surface is often approximated by the roughness criterion developed by Rayleigh (Beckmann and Spizzichino, 1963). According to the Rayleigh criterion, a surface is smooth if the standard deviation of the surface heights (also called "rms" height) of its irregularities, h, is

$$h < \frac{\lambda}{8 \sin \gamma}$$

where γ is the angle between the ground and the incident radar wave (defined as the "grazing" angle; for flat terranes, γ is equal to the complement of the incidence angle). Applying this criterion to the 28°- and 48°-incidence angles of the SIR-B data, the theoretical boundary between smooth and rough surfaces should have irregularities less than about 3 cm and 4.4 cm in height, respectively.

Table 2 shows standard deviation and maximum vertical relief values derived from measurements of surface roughness at seven sites along the length of the December 1974 lava flow (Fig. 12A). Measurements were made along 7- to 9-m-long transects using a templet, or surface simulator, with freely moving vertical rods spaced at 1-in. intervals (Gaddis and

TABLE 2. TEMPLET MEASUREMENTS OF SURFACE ROUGHNESS OF THE DECEMBER 1974 LAVA FLOW

Site	Standard deviation (cm)	Maximum vertical relief (cm)
A	1.9	9.9
B	2.9	15.9
C	4.8	26.2
D	5.2	23.5
E	9.8	52.4
F	13.4	56.3
G	21.9	90.8

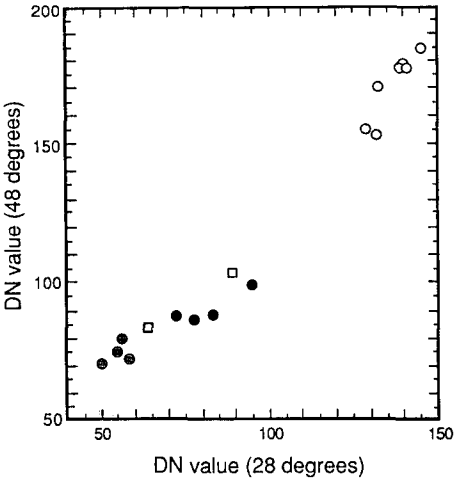

Figure 13. Pixel-brightness (data number, DN) values extracted from pahoehoe (filled circles) and a'a (open circles) lava flows, and ash (squares) deposits on the SIR-B images acquired at 48°- and 28°-incidence angles.

others, unpub. data). Note that although surface roughness generally increased along the flow length, five of these sites (A to E) were located in the pahoehoe portion of the flow, with the last two located on newly developed (F) and well-developed a'a (G). We see that the first three sites, A through C, have measured roughnesses less than or comparable to the 3 and 4.4 cm of the Rayleigh model and in fact are observed to be dark, or "radar smooth," on the SIR-B image (Fig. 12B). Measured roughnesses at sites D and E, located in the zone of transition between pahoehoe and a'a, are higher (about 5 to 10 cm), and examination of the SIR-B image of the December 1974 flow shows that the radar backscatter in these areas is indeed higher than that of the sites located within the smoother pahoehoe nearer the vent. The very bright return observed on the SIR-B image of this flow corresponds to a measured surface roughness for the a'a flow portion of greater than about 10 cm.

These comparisons between measured flow-surface roughness and radar backscatter suggest that the SIR-B data might be used as a "texture map" which reflects flow-surface textural changes produced by variations in lava rheological properties along the length of a lava flow. Although work is currently under way to determine the correlation between surface textures (as measured in the field) and emplacement characteristics of lava flows (Gaddis and others, unpub. data), more effort needs to be directed toward understanding the relationship between ground-surface textures and radar-image textures. In the following section, we present a comparison of the two SIR-B incidence angles for volcanic landform analysis near Kilauea, and the results of our efforts to enhance discrimination of geologic units, particularly the lava flows which dominate the surface area of Kilauea, on the SIR-B data. Enhancements utilized here include image smoothing, and mapping of image units on the basis of both average pixel brightness values (called "unit mapping" here) and the distribution of tonal variations (or "textures") within an image.

SIR-B IMAGE ENHANCEMENT FOR GEOLOGIC ANALYSIS

SIR-B Incidence Angle Comparison

A major SIR-B mission objective was to acquire digital radar images over the same target area at multiple angles of incidence (Cimino and others, 1986), in part to determine what types of geologic information could be derived from multi-incidence-angle data and to assess the utility of such data for structural analyses and lithologic mapping (Elachi and others, 1986). One purpose of this analysis is to compare lithologic mapping information obtained from the 28°- and 48°-incidence angle SIR-B images of Hawaii. Here we examine the relationship between the radar angle of incidence and the expected return signal level, and we present one approach for obtaining relative calibration between different radar measurements.

From the average trends of the backscatter curves of Figure 2, the incidence angle is observed to influence the signal level returned (backscatter) from a given unit area. As the amount of electromagnetic power returned to a radar is proportional to the scattering coefficient (that is, scattering area) of a target, for geologic targets larger than a radar resolution cell, the scattering area is replaced by an area-independent measure known as the "differential scattering coefficient," or "sigma zero" (σ^0). We therefore use average backscatter curves for theoretical expectations from SIR-B, and thus we expect that the average return at 28° should exceed the average return at 48°.

Figure 2 also illustrates the influence of surface roughness on the backscatter from a given unit area; as shown by the decrease in slope with increasing roughness, the difference in backscatter intensity between progressively larger angles of incidence becomes smaller as surface roughness increases (Kaupp and others, 1982). Since smoother surfaces have a larger difference in backscatter between 28° and 48°, a greater degree of unit discrimination should be observed for smoother units versus rougher units on the SIR-B data. From the greater separation of the backscatter curves at larger incidence angles (Fig. 2), we also expect that the sensitivity to roughness is greater for the 48°-incidence angle SIR-B data.

Figure 13 shows a plot of the average pixel brightness values (or data numbers, DNs) of several geologic units (pahoehoe and a'a flows, and ash deposits) in the two SIR-B images of Kilauea. The average DNs were calculated from unit regions of 300 to 3,000 pixels^2 in size. For these regions, ages range from 5 to 60 yr for pahoehoe, 28 to 197 yr for pyroclastic deposits, and 13 to 67 yr for a'a (Holcomb, 1987). For accurate interpretation of this plot, it must be noted that the data plotted are derived from the SIR-B images, which are themselves the product of a complex technology involving (1) the SIR-B sensor (including transient power stability problems); (2) illumination geometry (28° or 48° angles of incidence); (3) volcanic unit characteristics (including surface roughness and dielectric constant); and (4) processing decisions and variables (radiometric calibration, look-averaging, histogram mapping, and so on). As shown by the upward bias (that is, the nonzero y-intercept) of the line through the points plotted in Figure 13, the over-all brightness level is greater for the 48° image, even though theoretical considerations indicate that the average backscatter was probably lower from any given lava unit at this incidence angle. This implies that the processing was different for the two images. Note also that the slope of the line from the origin through the data plotted in Figure 13 is greater than 45°, reflecting the greater spread among rougher units for the 48° data and among smoother units for the 28° data. This slope thus indicates that the 48°-incidence-angle data exhibit greater sensitivity to surface roughness. This trend (slope) thus conforms to our expectations, whereas the preceding trend (bias) was contrary to expectations; both conclusions arise from the image data themselves.

Care must be exercised when comparing these SIR-B data. Even when the imaging sensor works flawlessly and the backscatter conforms to

our theoretical assessment of the physics at the surface, the return signal must be mapped into an image, and there are an infinite number of ways to do this (Matthews and others, 1984). Although a mapping algorithm is often provided so that a user can derive data uncorrupted by mapping enhancements designed to improve interpretability of the image data, this does not guarantee that a complete and accurate calibration exists for the sensor for two or more scenes of interest. Without such calibration data, it is invalid to compare data quantitatively from two or more scenes except in the most general and subjective ways (for example, Feature A is brighter than B, and B is brighter than C in image 1; A is brighter than B, but C is brighter than B in image 2).

Meaningful comparison of data from the 28° and 48° SIR-B images is a difficult problem, especially because of the transient problem of the SIR-B sensor in power transmission stability caused by a metal chip in the transmission path (Cimino and others, 1986). One approach, after Derryberry and others (1986), attacks this problem so that the need for accurate calibration of the sensor and for detailed knowledge of the image-mapping algorithm is eliminated. To adopt this approach for comparison of the two SIR-B images of Kilauea, the DNs of the 28° data are defined as

$$DN_{(28°)} = A\ \sigma^0\ (\Theta_1) \tag{1}$$

and in the 48°-incidence-angle SIR-B data as

$$DN_{(48°)} = A\ B\ \sigma^0\ (\Theta_1) \tag{2}$$

where DN_Θ is the average image DN calculated over a small homogeneous region at incidence angle Θ, A is a scaling factor accounting for all sensor and processing variables introduced in collecting the 28° data and mapping it into an image, B is the relative calibration factor accounting for sensor and processing differences from the 28° data to create the 48° image, and $\sigma^0(\Theta_1)$ is the backscatter at local incidence angle Θ_1.

The relative calibration value B can be estimated by forming the ratio of equations 1 and 2 and calculating the result for a homogeneous region (more estimations calculated at various points over the image dynamic range will improve the estimate):

$$\frac{DN_{(48°)}}{DN_{(28°)}} = B\ \frac{\sigma^0_{(48°)}}{\sigma^0_{(28°)}} \tag{3}$$

where $DN_{(48°)}$ and $DN_{(28°)}$ are the average DNs recorded for the same small homogeneous region in both images. Knowing B allows us to estimate A for the same regions in both images. For the 28° image, we use equation 1; for the 48° image, we use equation 2. If the assumptions are valid, realistic estimates of A and B are derived, providing a means of comparing uncorrupted data.

Using known σ^0 data for the ocean as a calibration point, A and B can be estimated. Ocean data were collected by the Naval Research Laboratory (NRL) in July 1965 (Guinard and Daley, 1970) using a scatterometer operating at L-band with horizontal polarization, as was SIR-B. Qualitatively, the NRL data matched the sea state near Hawaii at the time of the SIR-B overflights. Using the NRL data as estimates for σ^0 at 28°- and 48°-incidence angles in equation 3 and the average DNs from each image for ocean data, we calculated the relative calibration constant B to be

$$B = 9.72\ \text{dB} \tag{4}$$

and A to be

$$A = 59.37\ \text{dB}. \tag{5}$$

Equations 1 and 2 and the calibration constants 4 and 5 were used to derive data shown in Table 3 and Figure 14 for several Kilauea a'a and pahoehoe flows for the 28° and the 48° SIR-B images. These data show that the backscatter range for a'a was about 1 dB in both images, which was not apparent from the equivalent range of DNs for these flows. Note also the difference of about 7.8 dB in the a'a backscatter values at 28° compared to those at 48° (comparing the midpoint values), which was again not apparent from the DNs. In addition, these data show that the range of backscatter for pahoehoe was 5.4 dB in the 28° data and 2.7 dB in the 48° data. Comparing midpoint values, there is a difference of about 8.2 dB between the pahoehoe backscatter at 28° and the backscatter at 48°. Several conclusions can be drawn from these data.

1. The 28° incidence angle returned more signal power to the antenna than did the 48° incidence angle data, as shown by the σ^0 values

TABLE 3. DATA NUMBER (DN) AND SIGMA ZERO (σ^0, dB) VALUES FROM SIR-B DATA FOR SELECTED KILAUEA VOLCANO LAVA FLOWS

			A'a	Pahoehoe
28°	DN	Min.	130	50
		Max.	145	93
		Range	15	43
	σ^0	Min.	-17.90	-25.39
		Max.	-16.14	-20.00
		Range	0.95	5.39
48°	DN	Min.	160	72
		Max.	184	98
		Range	24	26
	σ^0	Min.	-25.01	-31.94
		Max.	-23.79	-29.27
		Range	1.22	2.67

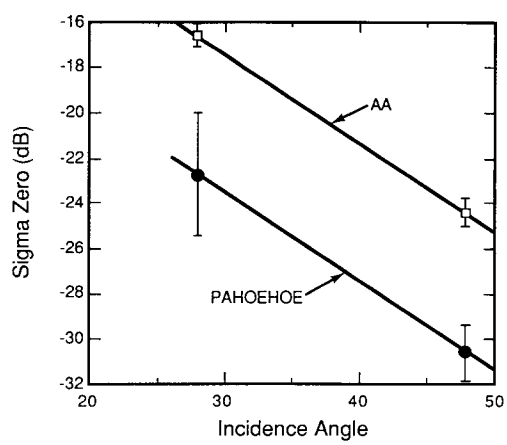

Figure 14. Radar backscatter (sigma zero, dB) versus incidence angle (degrees) from the SIR-B data of Kilauea for a'a and pahoehoe flows shown in Figure 13 and Table 3 at 28°-and 48°-incidence angles. The slopes of the lines drawn through the midpoint values are 0.391 dB/degree for a'a and 0.395 dB/degree for pahoehoe.

derived from the DNs recorded, and as expected from theoretical considerations. The 48° DNs represent a brighter image, however.

2. The rough surface of the a'a lava returned more power at both angles than did the smoother pahoehoe surface, and the range of variation was smaller between the angles for a'a than for pahoehoe, as expected. The first of these points is confirmed in the image DNs, but the second is not as obvious.

3. The 28° image shows a greater degree of unit discrimination among smoother units, as shown by a 5.4 dB range compared with the 48° pahoehoe data (2.7 dB range) and with a'a data at both incidence angles. This conclusion is consistent with observations based on DNs.

4. The bright, rough a'a lavas have about the same discriminability in both images as shown by a 1.0 dB range. Obviously we assume that the actual range of surface conditions is about the same for both a'a and pahoehoe flows under discussion.

5. The total range is about 9.3 dB from the brightest a'a to the darkest pahoehoe at 28° and about 8.2 dB at 48°. This means that the 28° imaging scenario produces data requiring a larger display dynamic range and thus reduced contrast on a pixel-to-pixel basis. Although our analysis of the DNs shows the opposite to be true, we conclude that the display dynamic range is greater for the 48° data, not the backscatter dynamic range.

6. The calculated σ^0 values show the 28° imaging configuration to be the more powerful one, with greater sensitivity, better unit discriminability, larger dynamic range, and producing data with a larger signal-to-noise ratio (that is, improved data quality). The same conclusion can be drawn from the DNs, but it would be based on weak inferences and misleading results.

It is important to note that an imaging radar with sufficient transmitter power and antenna and receiver gain can be tuned to discriminate radar-dark or radar-bright units. In fact, with sufficient dynamic range, a system could be tuned to discriminate both bright and dark units. When a system has marginal gain and range, all bright targets may be truncated and all dark ones buried in the noise. The linear distribution of the DNs plotted in Figure 13 suggests that SIR-B had sufficient gain and dynamic range available during acquisition of both the 28° and 48° images.

The greater degree of unit discrimination among smoother units on the 28° data can be observed in the map and 28° and 48° SIR-B images of Kilauea Caldera shown in Figure 10. In the 28° image (Figure 10B), the brightness contrast between the pahoehoe flows of July 1974 and 1919 is much greater than in the 48° image (Fig. 10C), thus enhancing our ability to distinguish between these units on the 28° image. Note that although the contrast in DNs between the July 1974 and the 1919 pahoehoe lava flows permits their separation to some degree on both images, the September 1982 pahoehoe flow (with DN's similar to those of the July 1974 flow) cannot be distinguished readily from either the adjacent 1921 pahoehoe flow or from deposits of the nearby 1790 pyroclastic ash. Thus we see that unambiguous distinction based on average DNs between many recent pahoehoe lava flows and pyroclastic deposits is difficult in the original digital SIR-B data. In the following sections, we examine the utility of several image-enhancement and analysis techniques for increasing our ability to distinguish between these smooth, radar-dark units.

Image Smoothing and Unit Mapping

To improve our ability to distinguish between low-return volcanic units on the SIR-B images, we have utilized two image-enhancement techniques on these digital data: image smoothing and unit mapping. Kilauea Caldera is chosen again as an example because its surface is dominated by low-return volcanic units such as pahoehoe flows and ash deposits. Image-smoothing techniques (specifically, mean and median filtering) were used to remove "speckle," or the mottling effects of spurious bright pixels. Speckle, an artifact of the radar-imaging process, is produced by random constructive and destructive interference of coherent radar energy (Goodman, 1976; Tomiyasu, 1983). Speckle produces an artificially granular or mottled image texture (that is, reduces the image quality and interpretability), and therefore removal of this effect is an important step in radar-image analysis. A common method of dealing with the problem of speckle involves the averaging of several radar "looks" (a look is a single "view" of a target along the ground swath). As multiple-look averaging has the combined effect of decreasing the amount of speckle and reducing the image resolution, a trade-off which optimizes these two parameters involves the averaging of four radar looks (Li and Bryan, 1983). Although this technique improves image quality while retaining much of the spatial resolution, the residual speckle continues to hamper quantitative image analysis, particularly image classification. For the SIR-B experiment, a compromise was achieved between the number of looks (4) and spatial resolution (about 25 m) (Curlander, 1986).

In order to further reduce the problem of speckle, both mean- and median-value filtering of four-look radar images have been employed (Blom and Daily, 1982). These filtering techniques utilize an odd-pixel–sized sliding "window" of pixels within which is calculated the mean or median value for all enclosed pixels; the center pixel is then replaced by the value calculated for that window (Pratt, 1978). For quantitative image analysis, Blom and Daily (1982) recommended the use of a median-value filter; although median-value calculation is more computer-intensive, the result is less affected by the presence of an unusually bright or dark pixel. Both a mean and median filter were applied to the SIR-B images of Kilauea Caldera, with 3×3, 5×5, 7×7, and 9×9 pixel window sizes used. Qualitative comparison of the two sets of filtered images indicated minimal differences in image quality; thus the less expensive, faster mean filter was preferred for our image analyses of the SIR-B data. Although for each set of images the 7×7 window size was judged the most useful for retaining spatial resolution while controlling speckle, the 9×9 window size produced smoother unit boundaries and internal image textures. As described below, the 9×9 mean filtered images are preferred for image analyses, such as unit mapping, texture analysis, or classification, which are dependent upon uniform unit signatures.

The value of radar image smoothing is illustrated in Figure 15, which shows mean-filtered versions of the 28° and 48° SIR-B images of Kilauea Caldera. These images were produced with a 7×7–pixel moving window. Note that the filtered images appear less "noisy" than do the images of Figure 10, with more uniform image textures and smoother unit boundaries (although the loss of image resolution is apparent even for this size of filter).

To aid the identification of geologic units within Kilauea Caldera, we utilized a technique referred to here as "unit mapping" (also called density slicing and gray-level quantization). This technique uses the image histogram (distribution of gray levels) to remap DNs in selected ranges or bins to common gray-level values. Image features with similar DNs may thus be remapped as the same "unit," the dimensions of which depend on the sizes of the bins selected. Figure 16 shows the results of using this technique on the SIR-B images of Kilauea Caldera using four single-valued bins. To assess the value of this technique for low-return unit discrimination, the bin boundaries were chosen from mean DNs of pahoehoe lava flows and pyroclastic deposits on the floor of Kilauea Caldera. The unit-mapped images (Fig. 16) thus show more uniform DNs and more distinct boundaries between several pahoehoe units, including those of July 1974 and 1919, and those of September 1982 and 1921. The use of this technique, however, has not significantly improved our ability to separate the

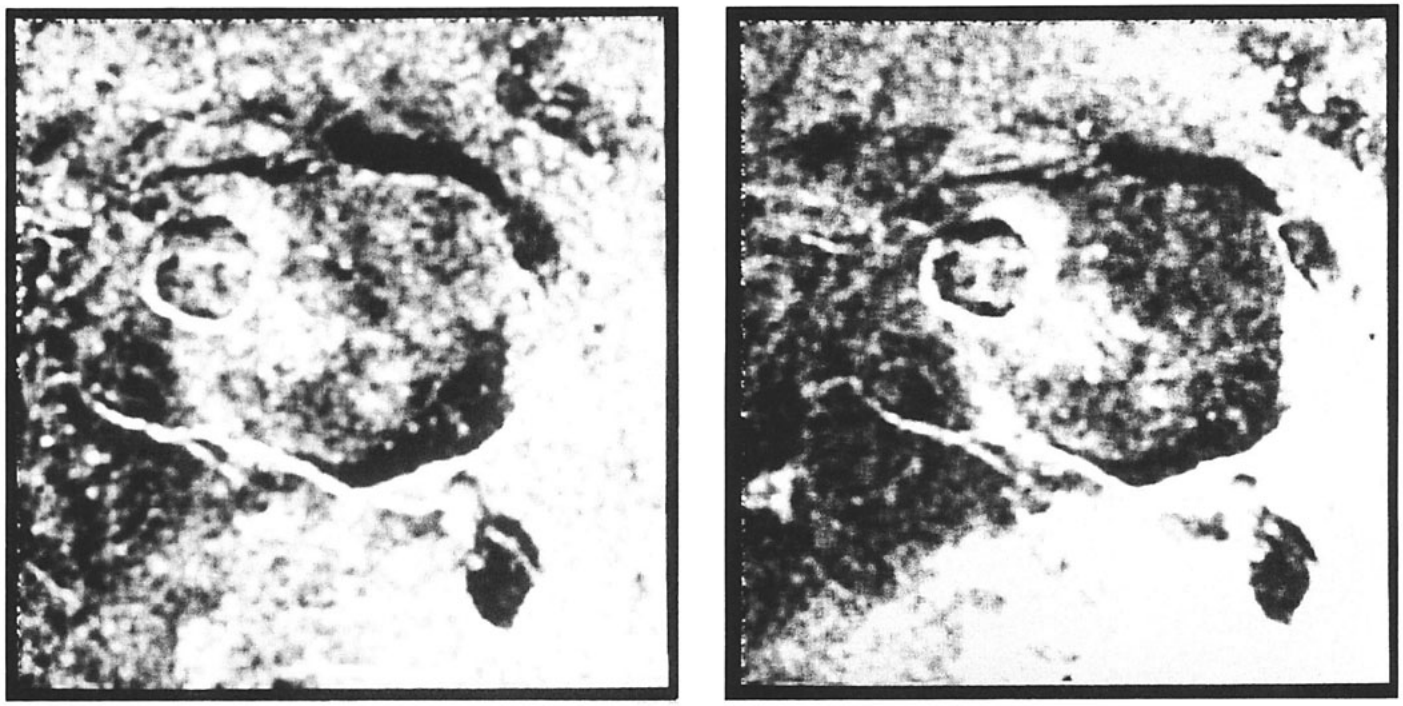

A B

Figure 15. Smoothed SIR-B images of Kilauea Caldera at incidence angles of (A) 28° and (B) 48°. These images were derived using a 7×7-pixel moving window within which the mean pixel value is calculated and substituted for the value of the center pixel.

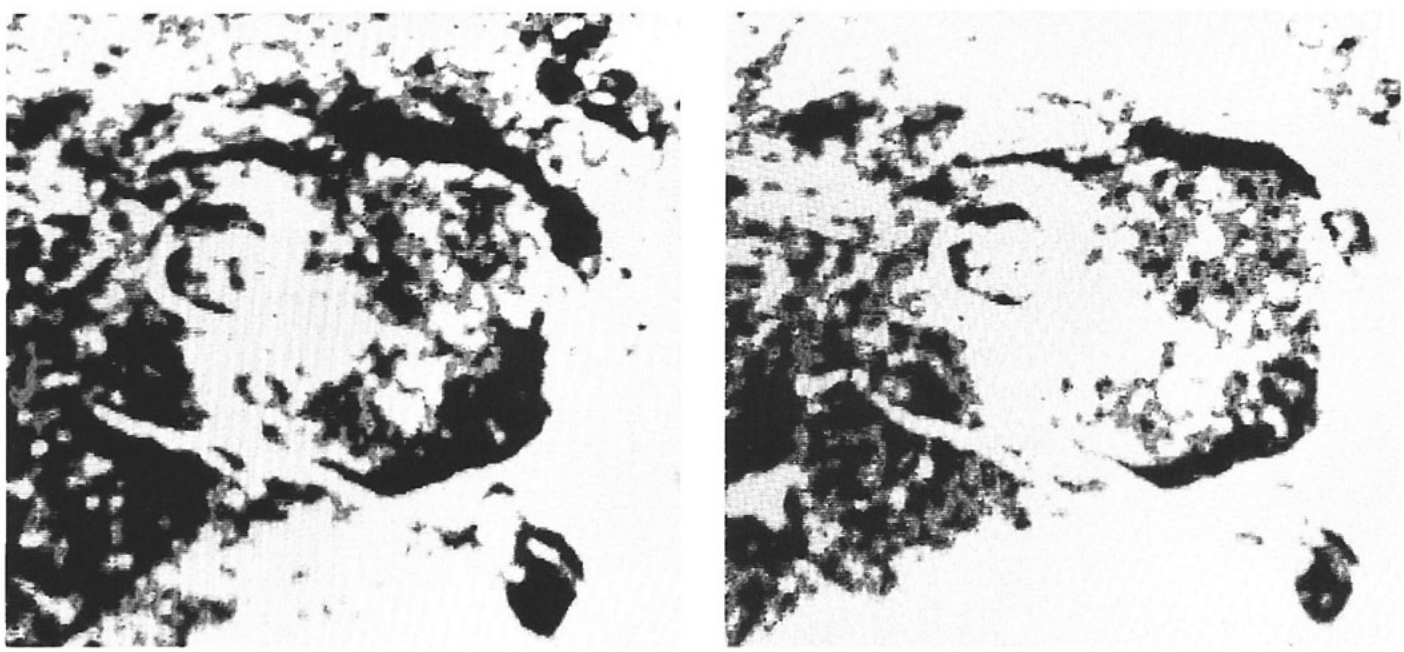

A B

Figure 16. Unit-mapped SIR-B images of Kilauea Caldera: (A) 28°-incidence-angle image; (B) 48°-incidence-angle image. These unit-mapped images were derived using four single-valued bins, with bin boundaries chosen on the basis of the mean pixel values of pahoehoe flows and pyroclastic deposits on the floor of Kilauea Caldera.

September 1982 pahoehoe flow and the 1790 ash deposit. In addition, note that since the bin values were primarily determined on the basis of DN ranges within low-return geologic units (that is, pahoehoe flows and ash deposits), the high-return units are saturated and expanded in size in these images. These examples show that although remapping of pixels on the basis of their average DN values serves to enhance unit boundaries, unambiguous low-return radar unit definition requires a significant separation in DNs (for example, larger than that observed for the 1790 ash deposit and September 1982 pahoehoe flow).

Texture Analysis

Although the unit-mapped images of Figure 16 improved discrimination of unit borders, and thus geologic unit mapping, optimal use of this technique requires knowledge of where the actual boundaries exist. A technique for unit separation which does not require user interpretation is based on unit textures in an image. Image "texture" is described as a measure of the spatial distribution of tonal variations in an image on a scale larger than the resolution element of the radar (Pratt, 1978). Texture analysis of image data has been used for many years (Haralick, 1979) and has been applied to a variety of geologic problems (Haralick and Shanmugam, 1974; Weszka and others, 1976; Irons and Peterson, 1981). Studies of radar image texture have shown that texture is an important spatial feature for identification and characterization of units in a radar image (Shanmugam and others, 1981; Frost and others, 1984; Stromberg and Farr, 1986; Ulaby and others, 1986).

To evaluate texture analysis for discrimination of units on the SIR-B data, we have adapted the gray-tone spatial-dependency technique of Haralick and others (1973). This technique, which provides a practical and easily computable method of characterizing image textures for terrane classification (Weszka and others, 1976; Conners and Harlow, 1980), computes a set of "texture features" (statistical measures of textural characteristics) from a gray-level co-occurrence matrix calculated for a digital image. This matrix is an M by M array which describes the occurrence of gray-level pairs in an image given the joint probability of a pair of gray levels occurring in a given direction and separation, where M is the number of gray levels possible. We have calculated a nearest-neighbor, gray-level co-occurrence matrix (separation = 1 pixel) for a quantized version of the 28°-incidence angle SIR-B image of Kilauea Caldera in which the value of M is 20. Four statistical texture features described by Haralick and others (1973) were computed in both the horizontal and vertical directions from this matrix: (1) *angular second moment* (ASM) measures homogeneity; (2) *contrast* (CON) measures local gray-level variation; (3) *correlation* (COR) measures linear dependencies, or the resemblance between rows and/or columns; (4) *entropy* (ENT) measures randomness. Although Haralick and others (1973) calculated a series of single texture features for an image, we computed each of the features above within a 5×5–pixel sliding window on the original image, replaced the center pixel of that window with the computed value, and produced a derived image showing the local variation for each feature. Our examination of the derived images indicates the following.

1. Images calculated horizontally (across) and vertically (down) show small differences which appear to be related to the look direction (northwest to southeast) of the radar. The vertically calculated texture features have more distinct unit boundaries and fault scarps and thus appear to reflect the preferential enhancement of features oriented perpendicular to the radar look direction.

2. Only the ASM, CON, and ENT features show enhancement of

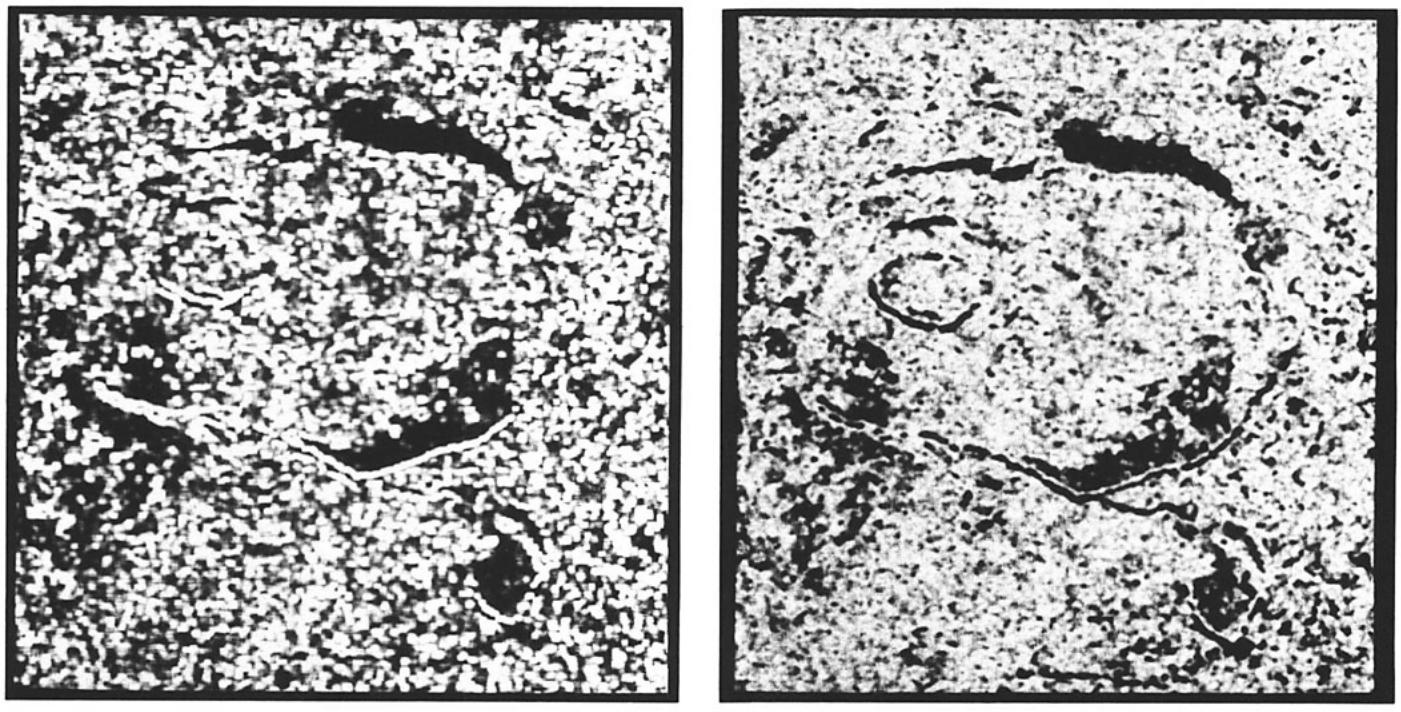

A B

Figure 17. Two image texture features calculated for the 28° SIR-B image of Kilauea Caldera using the algorithm of Haralick and others (1973): (A) shows the contrast feature; (B) shows the entropy feature. In these images, areas of high contrast and high entropy are shown as bright units, whereas areas with smooth image textures or relatively uniform pixel values are shown as dark units.

the young pahoehoe flows in the floor of Kilauea Caldera; the COR feature (similar to the original image but with degraded resolution) appears to reflect the lack of dominant long-wavelength topographic structure or trend in the original SIR-B image. Figure 17 shows the CON and ENT features calculated vertically for the 28° SIR-B data. In these images, areas of high contrast and high entropy (that is, large amounts of local brightness variation and randomness, respectively) are reproduced as bright units, whereas areas with relatively uniform pixel brightness values or smooth textures are shown as dark units. Comparison of these features for the September 1982 flow and the 1790 ash (see Fig. 10A), both shown as darker (more uniform) units surrounded by mottled areas of higher contrast and entropy, indicates that (aided by topographic enhancement of the south rim of the caldera) the September 1982 flow can indeed be distinguished as a separate unit on these images.

Our examination of the texture features calculated for the SIR-B data of Kilauea Caldera indicates that texture analysis does enhance discrimination of geologic units, particularly young pahoehoe flows, on the 28° SIR-B data. These results permit a few recommendations for texture analysis of radar images: (1) ASM and ENT features show similar but inverse results, suggesting that only one needs to be calculated as a measure of homogeneity; (2) calculation of texture features in only one direction, chosen to approximate the look direction of the radar, is recommended; (3) Haralick and others (1973) present additional texture features which might perform equally well or better than those used in our study.

GEOLOGIC ANALYSIS OF SIR-B DATA OF KILAUEA VOLCANO

To extrapolate the results of our geologic analysis of the SIR-B data of Kilauea to future SAR investigations of volcanic terranes, we must understand the extent to which SIR-B data can contribute to an interpretation of the eruptive history of Kilauea. In addition, an analysis of the eruptive history of Kilauea as it can be interpreted on the basis of the SIR-B data illustrates some of the advantages and limitations of radar data for geologic analysis of a volcanic terrane.

Kilauea Volcano has a number of features and units which are characteristic of basaltic shield volcanism, including a broad, gently sloping central cone that is commonly composed of numerous, thin basaltic lava flows; a summit crater or caldera complex; radial or concentric rifting and faulting; and associated lava flows, cinder cones, collapse pit craters, and smaller parasitic shields. Many of these landforms can be observed or inferred from examination of the SIR-B data. The existence of a gently sloping central shield can be inferred from observation of the bright rim of the large caldera complex and the southward (downslope) flow direction of flows along the SWRZ. The morphology of the observed summit caldera (surrounded by arcuate, overlapping faults, with associated pit craters) suggests multiple episodes of collapse, inferred to result from periodic withdrawal and perhaps explosive eruption of magma from an underlying chamber. The extensive low-return unit near the summit caldera indicates the presence of ash deposits and suggests that pyroclastic volcanism, at least in recent years, has been a major eruptive style in that area.

Radial faults and/or fissures are observed on the SIR-B data as faint bright traces trending southwest from the summit and as sites of numerous effusive eruptions. Many of the flows observed on the SIR-B data appear to originate from two centers of eruption along the SWRZ (Mauna Iki, the Great Crack). Several of these bright flows are superimposed on more broadly distributed, less bright (older?) flows, indicating that these eruptive centers may have evolved relatively recently, postdating eruptions occurring at other sites along the rift zone. Thus the recognition of parasitic vents and/or rift zones on radar images of volcanoes may be ambiguous, hindering studies of the internal structure of volcanic centers such as that of Nakamura (1977).

The numerous bright lava flows, interpreted to be a'a flows, provide evidence for effusive volcanism on the SIR-B images of Kilauea. Although radar data do not provide direct evidence of unit ages, variations in brightness for a'a flows suggest that relative ages may be inferred from their average brightness values (Derryberry and others, 1985; Farr, 1985). Such an approach assumes that the a'a flows were of similar surface roughness when they erupted and that the dominant influence on brightness is degradation by weathering (which must operate equally over the area studied); the brightening effect of vegetation growth with increasing age is usually ignored. On the assumption that this approach is valid for Kilauea, the brightest flows are interpreted to be the youngest, with brightness decreasing with increasing age (that is, as weathering progresses). Thus the observed variability in lava-flow brightness on the SIR-B images suggests that effusive volcanism has continued for some time, both predating and postdating a major explosive eruption of indeterminate age near the summit caldera. The approximately equal brightness of many flows, particularly near the smaller eruptive centers, indicates that they are coeval and that effusive eruptions were relatively frequent at these sites. The limited size and simple structure (that is, absence or limited number of flow lobes) of many flows also points toward the prominence of low-volume eruptions of short duration (Hulme, 1974; Moore and others, 1978; Baloga and Pieri, 1986). For example, the narrow, short (12-km-long), single-lobed December 1974 flow appears to have been formed by a short-duration eruption, whereas the longer, wider, multiple-lobed flows in the central and southwest SWRZ are suggestive of more complex, longer duration eruptive episodes. Such interpretations suggest that flow duration and complexity increased with increasing distance along the SWRZ, indicating the existence of a well-developed plumbing system between the summit and lower rift.

Although our SIR-B–based characterization of volcanism at Kilauea is generally accurate, misinterpretation of several aspects of the volcanic history of Kilauea would result from reliance upon the SIR-B data alone. As shown by an extensive dark unit and the apparent absence of pahoehoe flows, pyroclastic volcanism appears to be the dominant eruptive style at the Kilauea summit. In reality, large-scale explosive eruptions have been rare, and pyroclastic deposits cover only 2% of the present subaerial surface of Kilauea (Holcomb, 1987). The apparent lack of pahoehoe flows on the SIR-B data erroneously suggests that effusive eruption of these very fluid lavas was not common at Kilauea. In addition, because pahoehoe lavas often comprise the near-vent portions of longer flows, both the number of flows and the dimensions, especially the lengths, of many lava flows would be greatly underestimated. The apparent prevalence of a'a lavas along the rift zones also suggests that Kilauea lavas had higher average viscosities than they do and that the average eruption rate of Kilauea lavas were higher than they are (Rowland and Walker, 1989). Finally, the inability to distinguish features such as cinder cones, low-relief lava shields, and small fissure systems also mistakenly indicates that effusive or strombolian activity was a less important style of volcanism than large-scale pyroclastic eruptions.

In summary, we have shown that, compared to more conventional methods of geological reconnaissance such as field mapping and aerial photograph analysis, SIR-B has both advantages and limitations for the

geologic analysis of Kilauea volcanism. As discussed above, the directional nature of the SIR-B radar energy served to enhance large-scale topographic features such as the summit caldera and the Koae faults, which were oriented approximately perpendicular to the radar antenna. The sensitivity of the SIR-B radar to surface roughness has permitted delineation of the location and distribution of the rough-surfaced a'a lava flows of Kilauea. In addition, statistical information extracted from the digital data for these a'a lava flows may be used to constrain their relative ages (Derryberry and others, 1985) and flow-emplacement characteristics (Gaddis and others, unpub. data). Limitations of the SIR-B data for geologic analysis of Kilauea included the inability to resolve small-scale topographic features such as cinder cones and fissures, and the insensitivity to variations in small-scale roughness, resulting in an inability to separate pahoehoe flows from other low-return volcanic units.

The fact that many of these advantages and limitations were imposed by operating parameters of the SIR-B system suggests that future geologic analyses of SAR images of volcanic terranes could benefit from a critical evaluation of some of those parameters, particularly wavelength and incidence angle. The degree of surface roughness to which the SIR-B radar was most sensitive was influenced primarily by the 23-cm wavelength; although a'a lava flows were sufficiently rough to be enhanced on the SIR-B data, the smoother pahoehoe lavas were not distinguishable from adjacent, even smoother low-return units. The sensitivity of the radar to smaller-scale surface textural variations, and thus the detectability of pahoehoe lavas near Kilauea, might have been greatly improved if a smaller wavelength radar had been used. Because the use of a smaller wavelength would have resulted in the enhancement of both rougher pahoehoe and a'a lava flows, however, discrimination between these two flow types also would have been more difficult. Clearly the optimal choice of a single radar wavelength must depend on the nature of the surface to be studied; perhaps the best solution for Kilauea would have been to use multiple wavelengths.

The acquisition of SIR-B data at different or additional incidence angles might also have improved the discrimination of volcanic units near Kilauea. As illustrated in Figure 2, greater discrimination between geologic surfaces of differing roughness can be achieved by selecting incidence angles smaller than about 15° and greater than about 35°. For the 23-cm SIR-B radar, more appropriate incidence angles for the discrimination of voclanic units near Kilauea might have been closer to 20° and 50°.

CONCLUSIONS

Our examination of the SIR-B data of Kilauea Volcano has enabled us to draw the following conclusions regarding the use of SAR data for geologic analyses of volcanic terranes.

1. Several volcanic landforms of Kilauea, including large-scale tectonic features, the areally extensive 1790 pyroclastic deposit, and a'a lava flows, are readily observed and characterized on SIR-B images. Landforms with structures and/or surface textures on a smaller scale, such as cinder cones, spatter ramparts, fissures, and pahoehoe lava flows, were not well documented on the SIR-B data, however. Topographic features with greater than ~10 m of relief and radar-facing slopes were preferentially illuminated and thus enhanced on the radar images. Small-scale topographic features, with relief of less than 10 m, were not resolved on the SIR-B data. The smooth, generally fine-grained 1790 ash and the extremely rough a'a flow surfaces produced sufficiently low and high radar backscatter (respectively) in contrast to their surroundings that these two units were clearly identifiable on the SIR-B data. By contrast, the smooth pahoehoe flows produce dark returns which cannot be easily discriminated from those of other adjacent low-return units (for example, ash deposits).

2. Volcanic landform characterization does not vary significantly on the 28°- and 48°-incidence angle SIR-B images. With the uncalibrated digital data currently available to us, we can state only qualitatively that the SIR-B data acquired at a 28°-incidence angle provides slightly greater discrimination among the darker, low-return pahoehoe lava flows. For future radar missions, data obtained at incidence angles of about 15°–20°, 25°–35°, and 45°–50° would be more appropriate for volcanological investigations.

3. The use of standard image-enhancement techniques such as contrast enhancement, smoothing (pixel averaging), and unit mapping (density slicing), does not greatly improve discrimination among low-return units due to the inherently low signal strength. Although the use of statistical image texture analysis facilitated unit discrimination, the optimal use of this technique requires knowledge of the existence and characteristics of units to be distinguished.

4. Geologic analyses of the SIR-B data produced a generally accurate assessment of the character of Kilauea volcanism, indicating that radar data can provide a valuable means of studying less accessible volcanic terranes. Limitations of the SIR-B data, such as the difficulty in recognizing pahoehoe flows, however, result in the misinterpretation of several aspects of Kilauea volcanism. These observations suggest that caution should be exercised in the interpretation of SAR data of volcanic terranes.

ACKNOWLEDGMENTS

This research was funded by NASA Contract JPL 956925. The invaluable assistance of Scott Rowland, Cassandra Coombs, and Greg Coombs in collecting roughness measurements and of Joan Hayashi in programming is acknowledged gratefully. Thoughtful reviews by Baerbel Lucchitta and an anonymous reviewer were very helpful and were appreciated very much. The efforts of scientists and engineers who participated in the SIR-B mission are appreciated also, particularly those of the crew of Space Shuttle Flight 41-G, Mark Settle at NASA Headquarters, and the SIR-B Mission Support Team at the Jet Propulsion Laboratory. This research formed part of the dissertation in Geology and Geophysics of Gaddis at the University of Hawaii.

REFERENCES CITED

Baloga, S. M., and Pieri, D. C., 1986, Time-dependent profiles of lava flows: Journal of Geophysical Research, v. 91, p. 9543–9552.

Barsukov, V. L., and 29 others, 1986, The geology and geomorphology of the Venus surface as revealed by the radar images obtained by Veneras 15 and 16: Proceedings of the Lunar and Planetary Science Conference 16, Part 2: Journal of Geophysical Research, v. 91, p. D378–D398.

Basaltic Volcanism Study Project, 1981, Basaltic volcanism on the terrestrial planets: New York, Pergamon, 1,286 p.

Basilevsky, A. T., Pronin, A. A., Ronca, L. B., Kryuchkov, V. P., Sukhanov, A. L., and Markov, M. S., 1986, Styles of tectonic deformation on Venus: Analysis of Venera 15 and 16 data: Proceedings of the Lunar and Planetary Science Conference 16, Part 2: Journal of Geophysical Research, v. 91, p. D399–D411.

Beckmann, P., and Spizzichino, A., 1963, Electromagnetic scattering from rough surfaces: London, Pergamon Press.

Berlin, G. L., Tarabzouni, M. A., Al-Naser, A. H., Sheikho, K. M., and Larson, R. W., 1986, SIR-B subsurface imaging of a sand-buried landscape: Al Labbah Plateau, Saudi Arabia: IEEE Transactions on Geoscience and Remote Sensing, v. GE-24, no. 4, p. 595–602.

Blom, R., and Daily, M., 1982, Radar image processing for rock-type discrimination: IEEE Transactions on Geoscience and Remote Sensing, v. GE-20, no. 3, p. 343–351.

Blom, R., Elachi, C., and Evans, D., 1982, SIR-A radar images of sand dunes and volcanic fields: IEEE IGARSS, Munich, West Germany, p. 9.1–9.6

Campbell, D. B., Head, J. W., Harmon, J. K., and Hine, A. A., 1984, Volcanism and rift formation in Beta Regio: Science, v. 226, p. 167–170.

Carr, M. H., Greeley, R., Blasius, K. R., Guest, J. E., and Murray, J. B., 1977, Some Martian volcanic features as viewed from the Viking orbiters: Journal of Geophysical Research, v. 82, no. 28, p. 3985–4015.

Cimino, J., Elachi, C., and Settle, M., 1986, SIR-B—The second Shuttle Imaging Radar experiment: IEEE Transactions on Geoscience and Remote Sensing, v. GE-24, no. 4, p. 445–452.

Conners, R. W., and Harlow, C. A., 1980, A theoretical comparison of texture algorithms: IEEE Transactions on Pattern Analysis and Machine Intelligence, v. PAMI-2, no. 3, p. 204–222.

Curlander, J. C., 1986, Performance of the SIR-B digital image processing subsystem: IEEE Transactions on Geoscience and Remote Sensing, v. GE-24, no. 4, p. 649–652.
Decker, R. W., and Christiansen, R. L., 1984, Explosive eruptions of Kilauea Volcano, Hawaii, *in* Explosive volcanism: Inception, evolution, and hazards: Washington, D.C., National Academy of Science, p. 122–132.
Derryberry, B. A., Kaupp, V. H., MacDonald, H. C., Waite, W. P., Gaddis, L. R., and Mouginis-Mark, P., 1985, Introductory analyses of SIR-B radar data for Hawaii, *in* IEEE Digest, Proceedings of the 1985 International Geoscience and Remote Sensing Symposium, Amherst, Massachusetts, p. 370–375.
Derryberry, B. A., Waite, W. P., Kaupp, V. H., MacDonald, H. C., Gaddis, L. R., and Mouginis-Mark, P., 1986, Hawaiian lava flows and SIR-B results, *in* IEEE Digest, Proceedings of the 1986 International Geoscience and Remote Sensing Symposium, Zurich, Switzerland, September 1986, p. 497–501.
Elachi, C., Blom, R., Daily, M., Farr, T., and Saunders, R. S., 1980, Radar imaging of volcanic fields and sand dune fields: Implications for VOIR, *in* Radar geology: An assessment, Report of the Radar Geology Workshop, Snowmass, Colorado, JPL Publication 80-61, p. 114–150.
Elachi, C., Cimino, J., and Settle, M., 1986, Overview of the Shuttle Imaging Radar-B preliminary scientific results: Science, v. 232, p. 1511–1516.
Farr, T. G., 1985, Age-dating volcanic and alluvial surfaces with multipolarization data, *in* NASA/JPL Aircraft SAR Workshop Proceedings: JPL Publication 85-39, p. 31–36.
Farr, T. G., Elachi, C., Daily, M., and Blom, R., 1981, Imaging radar observations of volcanic features in Medicine Lake Highland, California, *in* IEEE Digest, Proceedings of the 1981 International Geoscience and Remote Sensing Symposium, Washington, D.C., p. 872–877.
Fielding, E., Knox, W. J., Jr., and Bloom, A. L., 1986, SIR-B radar imagery of volcanic deposits in the Andes: IEEE Transactions on Geoscience and Remote Sensing, v. GE-24, no. 4, p. 582–589.
Frost, V. S., Shanmugam, K. S., and Holtzman, J. C., 1984, The influence of sensor and flight parameters on texture in radar images: IEEE Transactions on Geoscience and Remote Sensing, v. GE-22, no. 5, p. 440–448.
Gaddis, L. R., Pieters, C. M., and Hawke, B. R., 1985a, Remote sensing of lunar pyroclastic mantling deposits: Icarus, v. 61, p. 461–489.
Gaddis, L. R., Mouginis-Mark, P. J., Kaupp, V. H., MacDonald, H. C., and Waite, W. P., 1985b, Preliminary geologic analyses of SIR-B radar data for Hawaii, *in* IEEE Digest, Proceedings of the 1985 International Geoscience and Remote Sensing Symposium, Amherst, Massachusetts, p. 364–367.
Goodman, J. W., 1976, Some fundamental properties of speckle: Optical Society of America Journal, v. 66, no. 11, p. 1145–1150.
Greenland, L. P., 1987, Hawaiian eruptive gases, *in* Volcanism in Hawaii, Volume 1: U.S. Geological Survey Professional Paper 1350, p. 759–770.
Guinard, N. W., and Daley, J. C., 1970, An experimental study of a sea clutter model: Proceedings of the IEEE, v. 58, no. 4, p. 543–550.
Haralick, R. M., 1979, Statistical and structural approaches to texture: Proceedings of the IEEE, v. 67, no. 5, p. 786–804.
Haralick, R. M., and Shanmugam, K., 1974, Combined spectral and spatial processing of ERTS imagery: Remote Sensing of Environment, v. 3, p. 3–13.
Haralick, R. M., Shanmugam, K., and Dinstein, I., 1973, Textural features for image classification: IEEE Transactions on Systems, Man, and Cybernetics, v. SMC-3, no. 6, p. 610–621.
Holcomb, R. T., 1980, Preliminary geologic maps of Kilauea Volcano, Hawaii: U.S. Geological Survey Open-File Report 80-796, 2 maps, scale 1:50,000.
——— 1987, Eruptive history and long-term behavior of Kilauea Volcano, *in* Volcanism in Hawaii, Volume 1: U.S. Geological Survey Professional Paper 1350, p. 261–350.
Holcomb, R. T., Champion, D., and McWilliams, M., 1986, Dating recent Hawaiian lava flows using paleomagnetic secular variation: Geological Society of America Bulletin, v. 97, p. 829–839.
Hulme, G., 1974, The interpretation of lava flow morphology: Royal Astronomical Society Geophysical Journal, v. 39, p. 361–383.
Irons, J. R., and Peterson, G. W., 1981, Texture transforms of remote sensing data: Remote Sensing of Environment, v. 11, p. 359–370.
Kaupp, V. H., Waite, W. P., and MacDonald, H. C., 1982, Incidence angle considerations for spacecraft imaging radar: IEEE Transactions on Geoscience and Remote Sensing, v. GE-20, p. 384–390.
Kaupp, V. H., Gaddis, L. R., Mouginis-Mark, P. J., Derryberry, B. A., MacDonald, H. C., and Waite, W. P., 1986, Preliminary analyses of SIR-B radar data for Hawaii: Remote Sensing of Environment, v. 20, p. 283–290.
Kieffer, H. H., Martin, T. Z., Peterfreund, A. R., Jakosky, B. M., Miner, E. D., and Palluconi, F. D., 1977, Thermal and albedo mapping of Mars during the Viking Primary Mission: Journal of Geophysical Research, v. 82, p. 4249–4291.
Kilburn, C.R.J., 1981, Pahoehoe and aa lavas: A discussion and continuation of the model of Peterson and Tilling: Journal of Volcanological and Geothermal Research, v. 11, p. 373–382.
Li, F. K., and Bryan, M. L., 1983, Tradeoffs among several synthetic aperture radar image quality parameters: Results of a user survey study: Photogrammetric Engineering and Remote Sensing, v. 49, p. 791–803.
Macdonald, G. A., Abbott, A. T., and Peterson, F. L., 1983, Volcanoes in the sea: Honolulu, Hawaii, University of Hawaii Press, 517 p.
Malin, M. C., Dzurisin, D., and Sharp, R. P., 1983, Stripping of Keanakakoi tephra on Kilauea Volcano, Hawaii: Geological Society of America Bulletin, v. 94, p. 1148–1158.
Masursky, H., Eliason, E., Ford, P. G., McGill, G. E., Pettengill, G. H., Schaber, G. G., and Schubert, G., 1980, Pioneer-Venus radar results: Geology from images and altimetry: Journal of Geophysical Research, v. 85, p. 8232–8260.
Matthews, N. D., Kaupp, V. H., Waite, W. P., and MacDonald, H. C., 1984, SAR image enhancement via post-correlation signal processing: IEEE Transactions on Geoscience and Remote Sensing, v. GE-22, no. 6, p. 582–585.
McCord, T. B., Clark, R. N., Hawke, B. R., McFadden, L. A., and Owensby, P. D., 1981, Moon: Near-infrared spectral reflectance, a first good look: Journal of Geophysical Research, v. 86, no. B11, p. 10883–10892.
Moore, H. J., Arthur, D.W.G., and Schaber, G. G., 1978, Yield strengths of flows on Earth, Mars, and moon: Lunar and Planetary Science Conference, 9th, Proceedings, p. 3351–3378.
Nakamura, K., 1977, Volcanoes as possible indicators of tectonic stress orientation—Principle and proposal: Journal of Volcanology and Geothermal Research, v. 2, p. 1–16.
Nakamura, K., Plafker, G., Jacob, K. H., and Davies, J. N., 1980, A tectonic stress trajectory map of Alaska using information from volcanoes and faults: Bulletin of the Earthquake Research Institute, v. 55, p. 89–100.
Peterson, D. W., and Tilling, R. I., 1980, Transition of basaltic lava from pahoehoe to aa, Kilauea Volcano, Hawaii: Field observations and key factors: Journal of Volcanological and Geothermal Research, v. 7, p. 271–293.
Pieters, C. M., 1978, Mare basalt types on the front side of the moon: A summary of spectral reflectance data: Lunar and Planetary Science Conference, 9th, Proceedings, p. 2825–2849.
Pieters, C., McCord, T. B., Zisk, S. H., and Adams, J. B., 1973, Lunar black spots and nature of the Apollo 17 landing area: Journal of Geophysical Research, v. 78, p. 5867–5875.
Pratt, W. K., 1978, Digital image processing: New York, John Wiley & Sons, 750 p.
Rowland, S. K., and Walker, G.P.L., 1989, Paired lava flows of Mauna Loa: Journal of Geophysical Research (in press).
Sabins, F. F., 1986, Remote sensing—Principles and interpretation (2nd edition): New York, W. H. Freeman and Company, 449 p.
Schaber, G. G., Thompson, T. W., and Zisk, S. H., 1975, Lava flows in Mare Imbrium: An evaluation of anomalously low Earth-based radar reflectivity: The Moon, v. 13, p. 395–423.
Schaber, G. G., McCauley, J. F., Breed, C. S., and Olhoeft, G. R., 1986, Shuttle Imaging Radar: Physical controls on signal penetration and subsurface scattering in the eastern Sahara: IEEE Transactions on Geoscience and Remote Sensing, v. GE-24, p. 603–623.
Shanmugam, K. S., Narayanan, V., Frost, V. S., Stiles, J. A., and Holtzman, J. C., 1981 Textural features for radar image analysis: IEEE Transactions on Geoscience and Remote Sensing, v. GE-19, p. 153–156.
Shaw, H. R., 1969, Rheology of basalt in the melting range: Journal of Petrology, v. 3, no. 3, p. 510–535.
Singer, R. B., 1985, Spectroscopic observation of Mars: Advances in Space Research, v. 5, no. 8, p. 59–68.
Stearns, H. T., 1985, Geology of the State of Hawaii (2nd edition): Palo Alto, California, Pacific Books, 335 p.
Stromberg, W. D., and Farr, T. G., 1986, A Fourier-based textural feature extraction procedure: IEEE Transactions on Geoscience and Remote Sensing, v. GE-24, no. 5, p. 722–731.
Tomiyasu, K., 1983, Computer simulation of speckle in a synthetic aperture radar image: IEEE Transactions on Geoscience and Remote Sensing, v. GE-21, p. 357–363.
Ulaby, F. T., Moore, R. K., and Fung, A. K., 1981, Microwave remote sensing: Active and passive, Volume I: Microwave remote sensing fundamentals and radiometry: Reading, Massachusetts, Addison-Wesley.
——— 1982, Microwave remote sensing: Active and passive, Volume II: Radar remote sensing and surface scattering and emission theory: Reading, Massachusetts, Addison-Wesley, 456 p.
Ulaby, F. T., Kouyate, F., Brisco, B., and Williams, T.H.L., 1986, Textural information in SAR images: IEEE Transactions on Geoscience and Remote Sensing, v. GE-24, no. 2, p. 235–245.
Walker, G.P.L., 1973, Explosive volcanic eruptions—A new classification scheme: Sonderdruck aus der Geologischen Rundeschau, v. 62, p. 431–446.
Wentworth, C. K., 1938, Ash formations of the isle of Hawaii: Hawaiian Volcano Observatory, Third Special Report, 183 p.
Wentworth, C. K., and Macdonald, G. A., 1953, Structures and forms of basaltic rocks in Hawaii: U.S. Geological Survey Bulletin 994, 98 p.
Weszka, J., Dyer, C., and Rosenfeld, A., 1976, A comparative study of texture measures for terrain classification: IEEE Transactions on Systems, Man and Cybernetics, v. SMC-6, p. 269–285.
Wood, C. A., 1984, Calderas: A planetary perspective: Journal of Geophysical Research, v. 89, no. B10, p. 8391–8406.
Zisk, S. H., Hodges, C. A., Moore, H. J., Shorthill, R. W., Thompson, T. W., Whittaker, E. A., and Wilhelms, D. E., 1977, The Aristarchus-Harbinger region of the Moon: Surface geology and history from recent remote sensing observations: The Moon, v. 17, p. 59–99.

Manuscript Received by the Society September 11, 1987
Revised Manuscript Received June 27, 1988
Manuscript Accepted June 30, 1988
Hawaii Institute of Geophysics Contribution No. 2015 and Planetary Geosciences Publication No. 521